RSCPublishing Journal of
Materials Chemistry A

Nanoconfined ammonia borane in a flexible metal-organic framework Fe-MIL-53: clean hydrogen release with fast kinetics

SCHOLARONE™
Manuscripts

ARTICLE TYPE

Nanoconfined ammonia borane in a flexible metal-organic framework Fe-MIL-53: clean hydrogen release with fast kinetics†

Gadipelli Srinivas,*[a,b] Will Travis,[c] Jamie Ford,[a,b] Hui Wu,[a,d] Zheng-Xiao Guo,[c] and Taner Yildirim*[a,b]

We demonstrated the dehydrogenation behaviour of nanoconfined ammonia borane (AB) in Fe-MIL-53, a flexible metal-organic framework (MOF) by solid state thermolysis. We observed clean hydrogen release with fast kinetics at
10 **reduced temperatures.**

Introduction:

The search for efficient hydrogen storage materials that can enable a hydrogen powered society is one of the most intriguing subjects in recent years.[1-9] Among many known hydrogen storage
15 material families, ammonia borane (NH$_3$BH$_3$; AB) has been considered one of the most promising candidates for chemical hydrogen storage applications because of its high gravimetric hydrogen content of 19.6 wt%.[4-6] However, due to very slow dehydrogenation kinetics below 100 °C and the release of
20 detrimental by-products such as ammonia, borazine and diborane during dehydrogenation, AB is not a practical hydrogen store. Therefore, many efforts have been made to obtain faster hydrogen release and prevent unwanted by-product generation.[8-17] Generally, reducing the metal hydride particle size to the
25 nanoscale is an effective and interesting strategy for enhancing both the kinetics and the thermodynamic properties. However, hydrogen storage nanoparticles have poor cycling stability due to particle agglomeration and coarsening. These problems can be averted if the nanoparticles are confined within highly porous
30 scaffold materials. Indeed, recent studies indicated that nanoconfinement of hydrogen storage materials in porous scaffolds not only improves the dehydrogenation kinetics but also prevents unwanted by-product generation.[8-23] To date, a number of porous support materials have been investigated to obtain
35 metal-hydrides at the nanoscale. These include silica,[15] carbon allotropes[16,17] and metal-organic frameworks[8-13, 19-23] (MOFs). In particular, MOFs are the most promising scaffold materials because of their unique interior active metal-centres for AB binding and well defined and ordered pores.[24] The flexibility in
40 tuning pore shape and size coupled with the choice of metal centre are the key parameters to explore for nanoconfinement of AB in MOFs. Li et at. were first to show successful AB nanoconfinement in Y-based MOF with fast hydrogen release kinetics at reduced temperatures and highly suppressed by-
45 product release.[8] Later, our group reported a considerably increased AB loading (about 3 times more than AB loading in Y-MOF[8]) in a Mg-MOF-74 for a given 1:1 mol AB:metal ratio.[9] Recently, various types of MOFs have been successfully explored to confine various hydrogen storage materials, including AB,[8-13]
50 dimethylamine borane,[18] magnesium,[19] magnesium borohydride,[20] lithium borohydride,[21] and, sodium aluminium hydride.[22,23] In particular, so far only *rigid framework* MOFs have been used to nanoconfine hydride particles. To the best of our knowledge, there has been no study on the usage of *flexible*
55 *framework* MOFs[25] for the nanoconfinement of AB. The most interesting property of flexible MOFs is that the structure has the ability to adapt the pore openings to accommodate guest species.[25] In other words, the pores of the flexible MOFs can expand and contract upon guest molecule absorption and
60 desorption, respectively. This effect, also called "breathing", can produce a dramatic increase or decrease in cell volume without a loss of crystallinity or bond breaking. Apart from flexible framework, Fe-MIL-53 has also coordinatively saturated Fe-sites compared to unsaturated metal (Mg^{+2} or Zn^{+2}) sites in MOF-74 in
65 our earlier reports.[9,10] Thus, infiltrated AB molecules within the flexible MOF pores with saturated Fe^{+3} sites could be interesting because the flexible pore size controls the strength of the host-guest interactions.

In this study, we demonstrate the nanoconfinement of AB in
70 flexible pores of Fe-MIL-53 (AB-Fe-MIL). We present a detailed study of the dehydrogenation properties of the nanoconfined phase of AB. AB-Fe-MIL shows advantageous dehydrogenation properties with faster kinetics at reduced temperatures than pristine AB. Most importantly, the system release clean hydrogen
75 upon heating; the residual B and N complexes are trapped within the pores. We also discuss the possible reasons for the improved dehydrogenation properties of nanoconfined AB within the MOF pores.

80 **Experimental details:**

Fe-MIL-53 was solvothermally synthesized and activated according to the reported procedure.[25,26] AB was confined within the anhydrous MIL pores by solution blending in an inert atmosphere. For a given AB:Fe ratio, the required amount of AB
85 and activated MIL sample were mixed through anhydrous methanol and stirred for 6 hours at room temperature. The methanol was then dried under vacuum at room temperature for 24 hours to remove the excess methanol. The targeted AB:M ratio was reconfirmed by weighing the initial MIL and AB-MIL
90 after complete vacuum drying process. Samples with 0.5:1, 1:1, and 1.5:1 molar ratios of AB:Fe were prepared. Samples without AB were also prepared in the same way and labelled as 'control'

sample. The samples were stored and handled in a helium filled glove box before further characterization. Powder X-ray diffraction (XRD) was carried out on samples sealed in 1.0 mm glass capillaries with Cu Kα radiation. Fourier-Transform Infrared (FTIR) spectra were collected at room temperature from sample/KBr pellets. X-ray photoelectron spectroscopy (XPS) measurements were performed using Al Kα radiation on Thermo Scientific K-Alpha system.[27] The mass spectrometry (MS) measurements were obtained with a ThermoStar gas analysis system (Pfeiffer Vacuum) coupled to a SDT Q600 thermogravimetric analyzer (TA Instruments) between 25 °C and 200 °C at a heating rate of 2 °C per minute under N_2 atmosphere. The isothermal dehydrogenation kinetics at various constant temperatures were measured by volumetric and temperature programmed desorption (TPD) methods using a carefully calibrated Sievert apparatus.[28] The volumetric thermal desorption was done by maintaining the base pressure at 10 mbar and heating at a rate of 2 °C/min.

Results and discussion:

As shown in **Figures 1 and S1** (in the supporting information (SI)), the Fe-MIL-53 framework is composed of infinite inorganic chains of trans-corner-shared $[MO_4(OH)_2]$ octahedra cross-linked by 1,4-benzenedicarboxylate linkers.[23] This gives an open-framework structure with one-dimensional diamond-shaped pore channels running parallel to the inorganic chains. However, after synthesis, the pores are filled with residual solvent molecules. Therefore, the MOF samples are activated by heating to 200 °C under vacuum to obtain anhydrous pores. Once active, these MOFs are suitable for further guest molecule absorption and catalytic applications. As shown in **Figure 1**, the anhydrous form of Fe-MIL-53 exhibits a *narrow pore* structure. The powder XRD patterns of the samples before and after encapsulation of AB within flexible pores are shown in **Figure 1** and **Figure S1**. The unit cell parameters of Fe-MIL-53 did not change much after AB loading except a little increase in b-axis, resulting in a unit cell volume increase from ~900 $Å^3$ for initial Fe-MIL-53 to ~925 $Å^3$ for AB-Fe-MIL-53. The simulated XRD pattern of 0.5:1 AB-MIL-53 is based on atomic positions obtained from first-principles calculations (see SI). The AB loadings within the MOF pores are 6.5 wt%, 13 wt%, and ~20 wt% for the given 0.5:1, 1:1 and 1.5:1 molar ratio of AB:Fe loading, respectively. The 1:1 AB:Fe loading corresponds to 4 AB molecules per unit cell. The disappearance of the crystalline AB peaks in the XRD patterns up to 1:1 AB per metal loading suggests that the AB molecules are successfully intercalated in the nanopores of MOF. However, we observed a trace of crystalline AB in the 1.5:1 AB:Fe sample (represented by vertical dotted lines in **Figure 1**), indicating that the pores are completely filled and excess AB is crystallized outside the pores. Nanoconfinement of AB within the flexible MOF pores is further confirmed by FTIR spectroscopy (**Figure S2**). The FTIR spectra of AB-Fe-MILs show combined IR modes related to the MOF and AB. However, we only observe very narrow H–N and H–B antisymmetric stretching IR modes. This suggests that AB–AB intermolecular interactions are significantly reduced in AB-MILs, giving rise to sharp dispersionless phonons from confined AB molecular vibrations.

Figures 2 and S3 represents the isothermal dehydrogenation
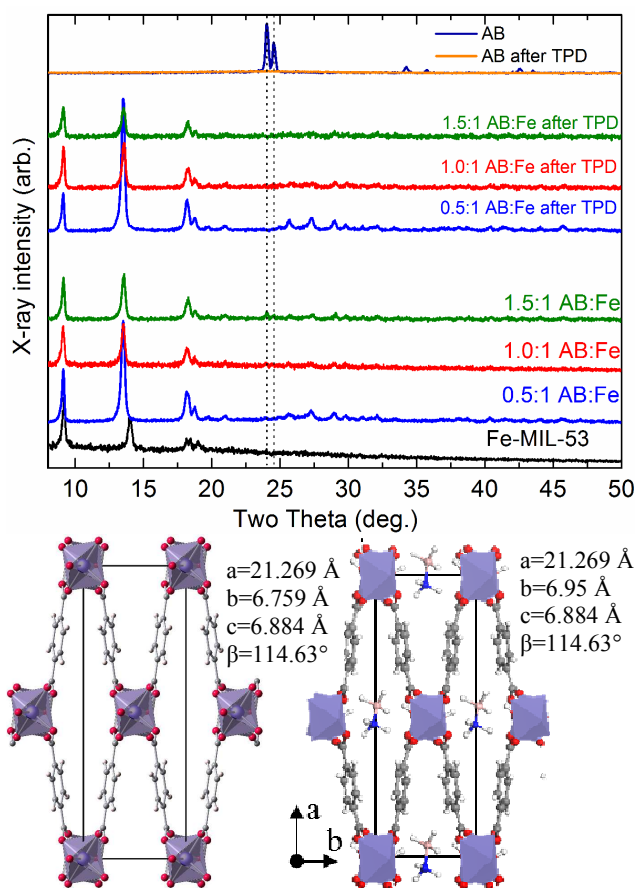
Fig. 1 Top: XRD patterns of the AB, Fe-MIL-53 and AB loaded Fe-MIL before and after thermal dehydrogenation. Bottom: very narrow pore structure and unit cell of Fe-MIL-53 and AB-Fe-MIL (0.5:1 AB:Fe) (gray C, red O, white H, blue B, and orange N)
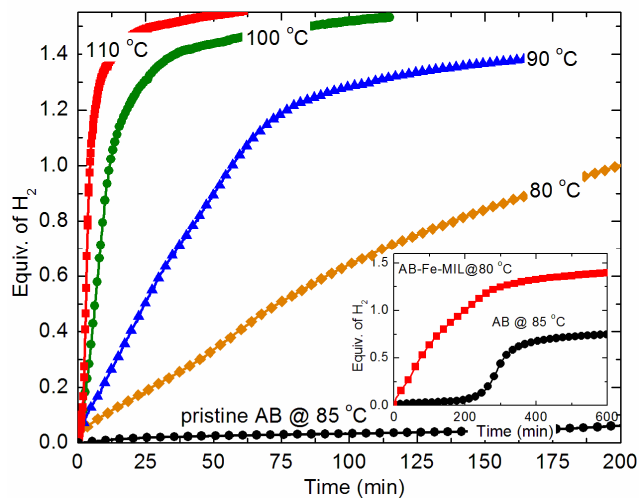
Fig. 2 Isothermal hydrogen desorption kinetics of AB-Fe-MIL-53 (1:1 AB:Fe) at different constant temperatures. For comparison, we also show 85 °C kinetics of pristine AB. Inset shows the prolonged time kinetics of AB-Fe-MIL-53 at 80 °C and pristine AB at 85 °C.

kinetics plots of AB-Fe-MIL-53 with 1:1 mol AB:Fe and 0.5:1 mol AB:Fe along with pristine AB. The amount of desorbed hydrogen is shown based on the AB within the MOF pores. Clearly, we obtain marked increase in dehydrogenation kinetics when compared to the pristine AB. AB-Fe-MIL exhibits faster

hydrogen release of 1.38 equiv. of H_2 around 100 °C within 30 minutes compared to an ultimate release of 0.84 equiv. of H_2 from pristine AB after a prolonged time (See **Figure S3**). More importantly, AB-Fe-MIL can release 1.22 equiv. of H_2 at 80 °C
5 even before pristine AB starts to decompose. In addition, AB-Fe-MIL shows instant H_2 release in contrast to the long incubation period in pristine AB.

To gain insight into the improved kinetics, we further determined the activation energy (E_a), from the temperature
10 dependence of dehydrogenation kinetics. The rate constant (k_T) of the dehydrogenation kinetics follows the inverse temperature dependence, which obeys the Arrhenius law, $k_T = k_° \exp(-E_a/RT)$. **Figure S4** represents the Arrhenius plots ($\ln(k_T)$ versus $1/T$) for AB-Fe-MIL samples with 0.5:1 AB:Fe and
15 1:1 AB:Fe loadings. The apparent activation energies for H_2 release are 130±7 kJ/mol and 135±3 kJ/mol for 0.5:1 AB:Fe and 1:1 AB:Fe loaded samples, respectively. This suggests that the energy barrier increases with increasing AB loading. The values are lower compared to the ~183 kJ/mol for the neat AB, thus
20 samples exhibit enhanced kinetics.[13,15]

The temperature programmed volumetric method is applied to see the dehydrogenation temperature and capacity of nanoconfined AB. **Figures 3** show the effect of AB loading on dehydrogenation temperature and kinetics. The thermal
25 desorption results indicate that increased AB loading increases the overall dehydrogenation temperature. Here it is worth noting that the AB-Fe-MIL systems exhibit reduced dehydrogenation temperature compared to the pristine AB. The TPD plot of the control sample indicates no residual methanol solvent left in the
30 MOF pores that can affect the dehydrogenated values of AB-loaded MOFs. The isothermal kinetics also becomes slow with higher AB loadings. We attribute this behaviour to increased AB–AB intermolecular interactions among the confined AB. When the pores have been overfilled, the formation of bulk AB
35 outside the pores further slows kinetics and increases the dehydrogenation temperature. The reduced AB particle size (defined by the pore size of support material) in very narrow pores have favourable desorption temperatures with rapid kinetics due to the increased surface area and decreased diffusion path
40 lengths. More importantly, the thermal desorption mass spectroscopy measurements on AB-Fe-MIL (**Figure S5**) reveals the clean hydrogen release by suppressing the generation of unwanted gases, such as ammonia, borazine and diborane. It is also worth to note that in contrast to neat AB, no foaming was
45 observed upon heating the AB-loaded MOF samples at temperatures up to 200 °C (**Figure S6**).

In order to understand the dehydrogenation behaviour of nanoconfined AB within the MOF pores, we further investigated the samples with XRD, FTIR and XPS tests before and after
50 thermal dehydrogenation at 200 °C. It is important to point out that XRD and FTIR data show the host MOF structure does not change after AB loading and thermal dehydrogenation (**Figures 1 and S2**). The change in XRD peak intensities upon AB incorporation in Fe-MIL-53 system indicates the disordered guest
55 AB molecules within the pores. The trapping of B− and N−containing residues within the MOF pores is evidenced from the unchanged XRD patterns of AB-Fe-MIL samples after thermal dehydrogenation. FTIR spectra reveal no evidence of

60
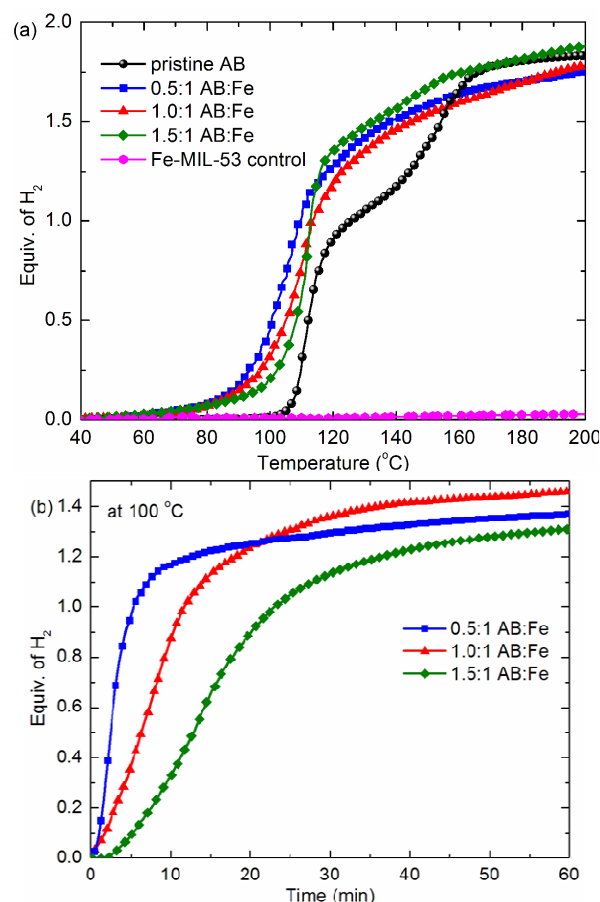
Fig. 3 The effect of increased AB loading in Fe-MIL-53 on the hydrogen desorption properties. (a) temperature programmed desorption (TPD) of hydrogen and (b) isothermal kinetics at 100 °C.
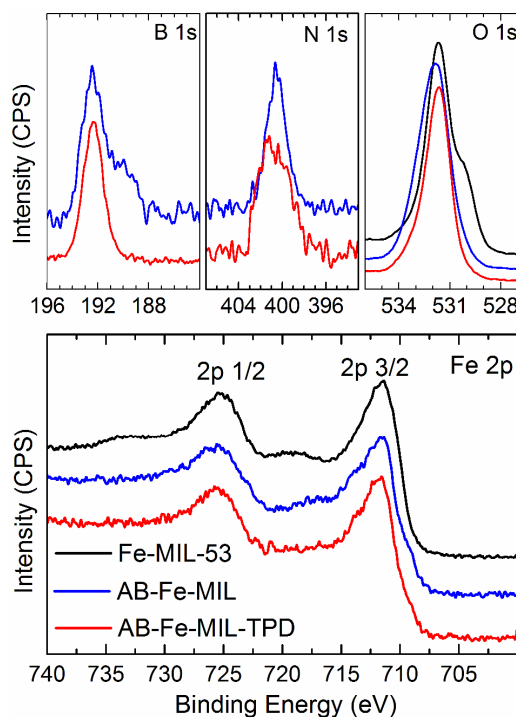
65 **Fig. 4 B 1s, N 1s, O 1s and Fe 2p core level XPS spectra of AB and AB-Fe-MIL (1:1 AB:Fe) before and after TPD runs. The Fe-MIL-53 is also included for comparison.**

B–H bonds in AB-Fe-MIL samples after thermal desorption. However, the N–H stretch is seen at ~3300 cm^{-1} in AB-Fe-MIL samples after thermal desorption. The appearance of additional IR modes is assigned to the B coordination with the surrounding O groups in the MOF pores (**Figure S2**).[9,10] Furthermore XPS results shown in **Figures 4 and S7** reveal the important and clear evidence for the improved thermal dehydrogenation behaviour of nanoconfined AB and trapped B− and N−residues within the MOF pores. The B 1s core level spectra before thermal desorption shows the highly destabilized B–H (binding energy, BE of ~188 eV) and B–N (BE ~190 eV) bonds and the new B–O bond (BE ~192 eV) in AB-Fe-MIL sample.[12,29,30] The complete brakeage of B–N bonds and much stronger B–O bond are seen after thermal desorption.[29,30] The N 1s core level spectra show formation of −NH$_2$–O and −NH$_2$–Fe groups (at BE ~400 eV and above) without evidence of B–N bonds (BE ~398 eV) or free amino groups (–NH$_2$).[29,31] The Fe 2p and O 1s core level spectra of Fe-MIL-53 show the characteristic iron(III) oxide peaks (see SI and **Figure S7**). In the AB-Fe-MIL and AB-Fe-MIL-TPD, the Fe 2p spectra resembles the Fe(II,III).[32,33] This is attributed to the interaction of −NH$_2$ groups with open Fe(III) centres. The −NH$_2$ interaction with O and Fe(III) is also evidenced from the relatively broad peak in N 1s spectra after thermal desorption.[31] It is important to note that no evidence is found for complete reduction of Fe(III) to metallic Fe(0). In conclusion, the observed AB decomposition at reduced temperatures and clean hydrogen generation without by-products is attributed to a combined effect of MOF pore O−functional groups and the unsaturated Fe(III) sites interaction with the electropositive B in −BH$_3$ and the electronegative N in −NH$_3$ groups of confined AB. The B–O bond formation destabilizes the B–H and B–N bonds to improve the thermal dehydrogenation kinetics and lower the dehydrogenation temperature. The complete suppression of B–H signal in FTIR and XPS spectra indicate the all H atoms at −BH$_3$ group are desorbed first (1.5 equivalents of H$_2$) during the thermolysis process.

Conclusion:

In summary, we demonstrated the successful nanoconfinement of AB molecules within the flexible MOF pores and studied the thermal dehydrogenation behaviour. We found that the encapsulation of AB in very narrow pores of Fe-MIL-53 has a large impact on the dehydrogenation temperature and kinetics. The results suggested that largely destabilized intermolecular bonds upon infiltration into the MOF pores, thus led to decreased dehydrogenation temperature and fast hydrogen release kinetics. Most importantly, the flexible pores also trapped the B- and N-containing residues to stop the release of by-products; ammonia, borazine, and diborane, thus yielding only clean hydrogen generation. When compared to the unsaturated metalMOFs,[8-10] the flexible pores in MIL-53 did not exhibit much improvements in hydrogen release kinetics and temperature, suggesting that the dehydrogenation property of confined AB is largely governed by coordinatively unsaturated metal sites in MOF pores. The findings reported here will help us in considering other support materials to tune the dehydrogenation properties of AB-MOF or other porous supports with desired hydrogen release kinetics and reversibility.
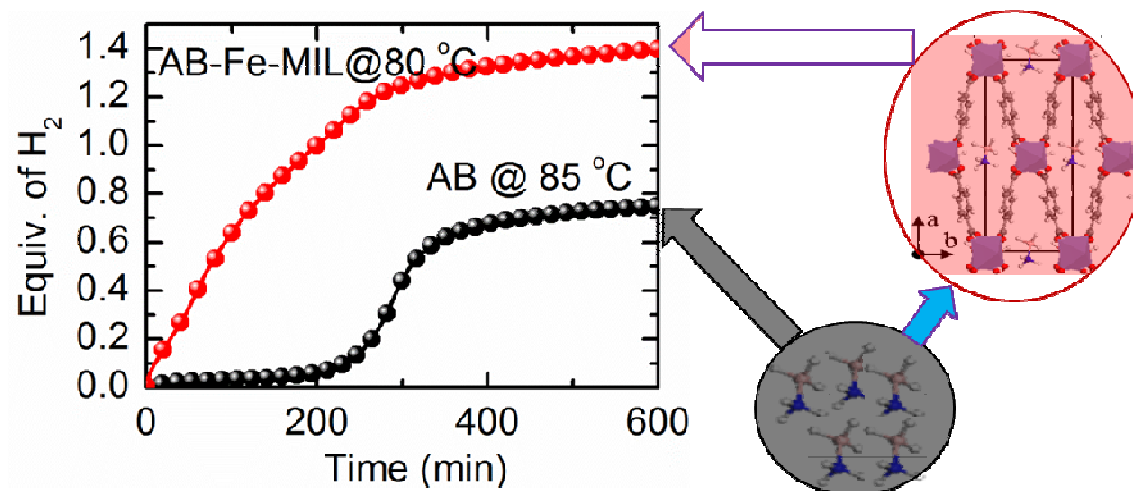
Notes and references

^{a} NIST Center for Neutron Research, National Institute of Standards and Technology, Gaithersburg, Maryland, 20899-6102 (USA). Fax: +1301-921-9847; Tel: +1301-975-6228; E-mail: taner@seas.upenn.edu (T. Yildirim) or gsrinivasphys@gmail.com (G. Srinivas).
^{b} Department of Materials Science and Engineering, University of Pennsylvania, Philadelphia, Pennsylvania, 19104-6272 (USA).
^{c} Department of Chemistry, University College London, 20 Gordon Street, London, WC1H 0AJ (UK).
^{d} Department of Materials Science and Engineering, University of Maryland, College Park, Maryland, 20742-2115 (USA).
† Electronic Supplementary Information (ESI) available: See DOI: 10.1039/b000000x/

1   C. Weidenthaler and M. Felderhoff, Solid-state hydrogen storage for mobile applications: quo vadis?, *Energy Environ. Sci.*, 2011, **4**, 2495-2502.
2   P. Jena, Materials for hydrogen storage: past, present, and future, *J. Phys. Chem. Lett.*, 2011, **2**, 206-211.
3   J. Yang, A. Sudik, C. Wolvertonb and D. J. Siegel, High capacity hydrogen storage materials: attributes for automotive applications and techniques for materials discovery, *Chem. Soc. Rev.*, 2010, **39**, 656-675.
4   A. D. Sutton, A. K. Burrell, D. A. Dixon, E. B. Garner III, J. C. Gordon, T. Nakagawa, K. C. Ott, J. P. Robinson and M. Vasiliu, Regeneration of ammonia borane spent fuel by direct reaction with hydrazine and liquid ammonia, *Science*, 2011, **331**, 1426-1429.
5   Z. Tang, H. Chen, X. Chen, L. Wu and X. Yu, Graphene oxide based recyclable dehydrogenation of ammonia borane within a hybrid nanostructure, *J. Am. Chem. Soc.*, 2012, **134**, 5464-5467.
6   F. Mertens, G. Wolf and F. Baitalow, Ammonia borane and related compounds as hydrogen source materials, in Handbook of hydrogen storage (Ed. M. Hirscher), 2011, Wiley-VCH Verlag GmbH & Co. KGaA, Weinheim, Germany. DOI: 10.1002/9783527629800.ch8.
7   A. Al-Kukhun, H. T. Hwang and A. Varma, A Comparison of ammonia borane dehydrogenation methods for proton-exchange-membrane fuel cell vehicles: hydrogen yield and ammonia formation and its removal, *Ind. Eng. Chem. Res.*, 2011, **50**, 8824-8835.
8   Z. Li, G. Zhu, G. Lu, S. Qiu and X. Yao, Ammonia borane confined by a metal-organic framework for chemical hydrogen storage: enhancing kinetics and eliminating ammonia, *J. Am. Chem. Soc.*, 2010, **132**, 1490-1491.
9   S. Gadipelli, J. Ford, W. Zhou, H. Wu, T. J. Udovic and T. Yildirim, Nanoconfinement and catalytic dehydrogenation of ammonia borane by magnesium-metal-organic framework-74, *Chem. Eur. J.*, 2011, **17**, 6043-6047.
10 G. Srinivas, J. Ford, W. Zhou and T. Yildirim, Zn-MOF assisted dehydrogenation of ammonia borane: enhanced kinetics and clean hydrogen generation, *Int. J. Hydrogen Energy*, 2011, **37**, 3633-3638.
11 R.-Q. Zhong, R.-Q. Zou, T. Nakagawa, M. Janicke, T. A. Semelsberger, A. K. Burrell and R. E. Del Sesto, Improved hydrogen release from ammonia-borane with ZIF-8, *Inorg. Chem.*, 2012, **51**, 2728–2730.
12 X.-L. Si, L.-X. Sun, F. Xu, C.-L. Jiao, F. Li, S.-S. Liu, J. Zhang, L.-F. Song, C.-H. Jiang, S. Wang, Y.-L. Liu and Y. Sawada, Improved hydrogen desorption properties of ammonia borane by Ni-modified metal-organic frameworks, *Int. J. Hydrogen Energy*, 2011, **36**, 6698–6704.
13 Y. Li, P. Song, J. Zheng and X. Li, Promoted H$_2$ generation from NH$_3$BH$_3$ thermal dehydrogenation catalyzed by metal-organic framework based catalysts, *Chem. Eur. J.*, 2010, **16**, 10887-10892.
14 Y. Peng, T. Ben, Y. Jia, D. Yang, H. Zhao, S. Qiu, X. Yao, Dehydrogenation of ammonia borane confined by low-density porous aromatic framework, *J. Phys. Chem. C*, 2012, **116**, 25694-25700.

15 A. Gutowska, L. Y. Li, Y. S. Shin, C. M. Wang, X. S. Li, J. C. Linehan, R. S. Smith, B. D. Kay, B. Schmid, W. Shaw, M. Gutowski and T. Autrey, Nanoscaffold mediates hydrogen release and the reactivity of ammonia borane, *Angew. Chem, Int. Ed.*, 2005, **44**, 3578-3582.

16 Z. Kurban, A. Lovell, S. M. Bennington, D. W. K. Jenkins, K. R. Ryan, M. O. Jones, N. T. Skipper and W. I. F. David, A solution selection model for coaxial electrospinning and its application to nanostructured hydrogen storage materials, *J. Phys. Chem. C*, 2010, **114**, 21201–21213.

17 T. K. Nielsen, F. Besenbacherb and T. R. Nanoconfined hydrides for energy storage, *Nanoscale*, 2011, **3**, 2086–2098.

18 S. B. Kalidindi, D. Esken and R. A. Fischer, B-N chemistry@ZIF-8: dehydrocoupling of dimethylamine borane at room temperature by size-confinement effects, *Chem. Eur. J.* 2011, **17**, 6594-6597.

19 D.-W. Lim, J. W. Yoon, K. Y. Ryu and M. P. Suh, Magnesium nanocrystalls embedded in a metal-organic framework: hybrid hydrogen storage with synergistic effect on physi- and chemisorption, *Angew. Chem. Int. Ed.*, 2012, **51**, 9814-9817.

20 M. J. Ingleson, J. P. Barrio, J. Bacsa, A. Steiner, G. R. Darling, J. T. A. Jones, Y. Z. Khimyak and M. J. Rosseinsky, Magnesium borohydride confined in a metal–organic framework: a preorganized system for facile arene hydroboration, *Angew. Chem., Int. Ed.*, 2009, **48**, 2012–2016.

21 W. Sun, S. Li, J. Mao, Z. Guo, H. Liu, S. Dou and X. Yu, Nanoconfinement of lithium borohydride in Cu-MOFs towards low temperature dehydrogenation, *Dalton Trans.*, 2011, **40**, 5673-5676.

22 R. K. Bhakta, J. L. Herberg, B. Jacobs, A. Highley, R. Behrens, Jr., N. W. Ockwig, J. A. Greathouse and M. D. Allendorf, Metal-organic frameworks as templates for nanoscale NaAlH$_4$, *J. Am. Chem. Soc.*, 2009, **131**, 13198–13199.

23 V. Stavila, R. K. Bhakta, T. M. Alam, E. H. Majzoub and M. Allendorf, Reversible hydrogen storage by NaAlH$_4$ confined within a titanium-functionalized MOF-74(Mg) nanoreactor, *ACS Nano*, 2012, **27**, 9807–9817.

24 A. Corma, H. García and F. X. Llabrés i Xamena, Engineering metal organic frameworks for heterogeneous catalysis, *Chem. Rev.*, 2010, **110**, 4606-4655.

25 F. Millange, N. Guillou, R. I. Walton, J.-M. Grenéche, I. Margiolakid and G. Férey, Effect of the nature of the metal on the breathing steps in MOFs with dynamic frameworks, *Chem. Commun.*, 2008, 4732-4734.

26 C. Scherb, A. Schödel and T. Bein, Directing the structure of metal–organic frameworks by oriented surface growth on an organic monolayer, *Angew. Chem.*, 2008, **120**, 5861-5863.

27 Certain trade names and company products are mentioned in this paper to adequately specify the experimental procedure and equipment used. In no case does this imply recommendation or endorsement by NIST, nor does it imply that the products are necessarily the best available for this purpose.

28 W. Zhou, H. Wu, M. R. Hartman, T. Yildirim, Hydrogen and methane adsorption in metal-organic frameworks: a high-pressure volumetric study, *J. Phys. Chem. C*, 2007, **111**, 16131-16137.

29 O. Baake, P. S. Hoffmann, A. Klein, B. Pollakowski, B. Beckhoff, W. Ensinger, M. Kosinova, N. Fainer, V. S. Sulyaevac and V. Trunova, Chemical character of BC$_x$N$_y$ layers grown by CVD with trimethylamine borane, *X-Ray Spectrom.*, 2009, **38**, 68–73.

30 J. Zhao, J. Shi, X. Zhang, F. Cheng, J. Liang, Z. Tao and J. Chen, A soft hydrogen storage material: poly(methyl acrylate)-confined ammonia borane with controllable dehydrogenation, *Adv. Mater.*, 2010, **22**, 394–397

31. Y. Wang, B. Li, Y. Zhou, D. Jia and Y. Song, CS-Fe(II,III) complex as precursor for magnetite nanocrystal, *Polym. Adv. Technol.*, 2011, **22**, 1681–1684.

32 T. Yamashita, P. Hayes, Analysis of XPS spectra of Fe^{2+} and Fe^{3+} ions in oxide materials, *Appl. Surf. Sci.*, 2008, **254**, 2441–2449.

33 X. Zhou, Z. Chen, D. Yan and H. Lu, Deposition of Fe–Ni nanoparticles on polyethyleneimine-decorated graphene oxide and application in catalytic dehydrogenation of ammonia borane, *J. Mater. Chem.*, 2012, **22**, 13506–13516.

A Table of contents entry

Nanoconfined ammonia borane (AB) in MOF pores offers clean hydrogen release and fast kinetics at reduced temperatures than bulk AB.

Nanoconfined ammonia borane in a flexible metal-organic framework Fe-MIL-53: clean hydrogen release with fast kinetics

Gadipelli Srinivas[a,b,]*, **Will Travis**[c], **Jamie Ford**[a,b], **Hui Wu**[a,d], **Zheng-Xiao Guo**[c] **and Taner Yildirim**[a,b,]*

[a]NIST Center for Neutron Research, National Institute of Standards and Technology, Gaithersburg, Maryland, 20899-6102 (USA).

[b]Department of Materials Science and Engineering, University of Pennsylbvania, Philadelphia, Pennsylvania, 19104-6272 (USA).

[c]Department of Chemistry, University College London, 20 Gordon Street, London, WC1 0AJ, (UK).

[d]Department of Materials Science and Engineering, University of Maryland, College Park Maryland, 20742-2115 (USA).

*Contact address: Fax: +1301-921-9847; Tel: +1301-975-6228; E-mail: gsrinivasphys@gmail.com (G. Srinivas); taner@seas.upenn.edu (T. Yildirim).
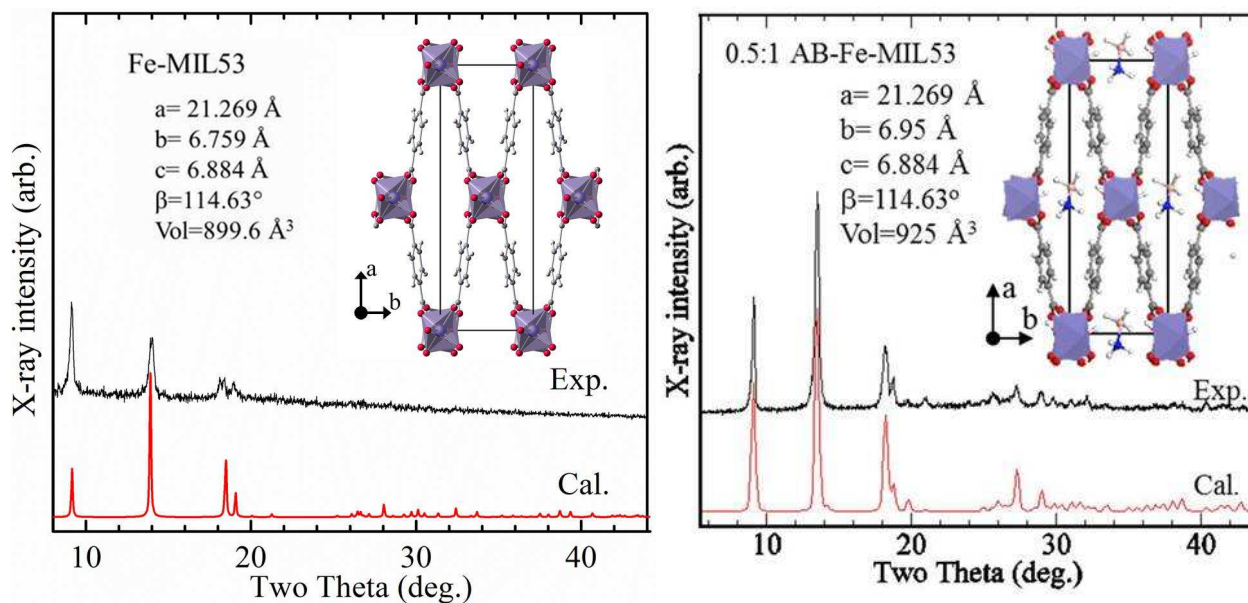
Figure S1. The measured and calculated XRD patterns of the bare Fe-MIL-53 and AB loaded Fe-MIL (0.5:1 AB:Fe). The inset shows the unit cell with very narrow pore structure and has C 2/c symmetry (gray C, red O, white H, blue B, and orange N).
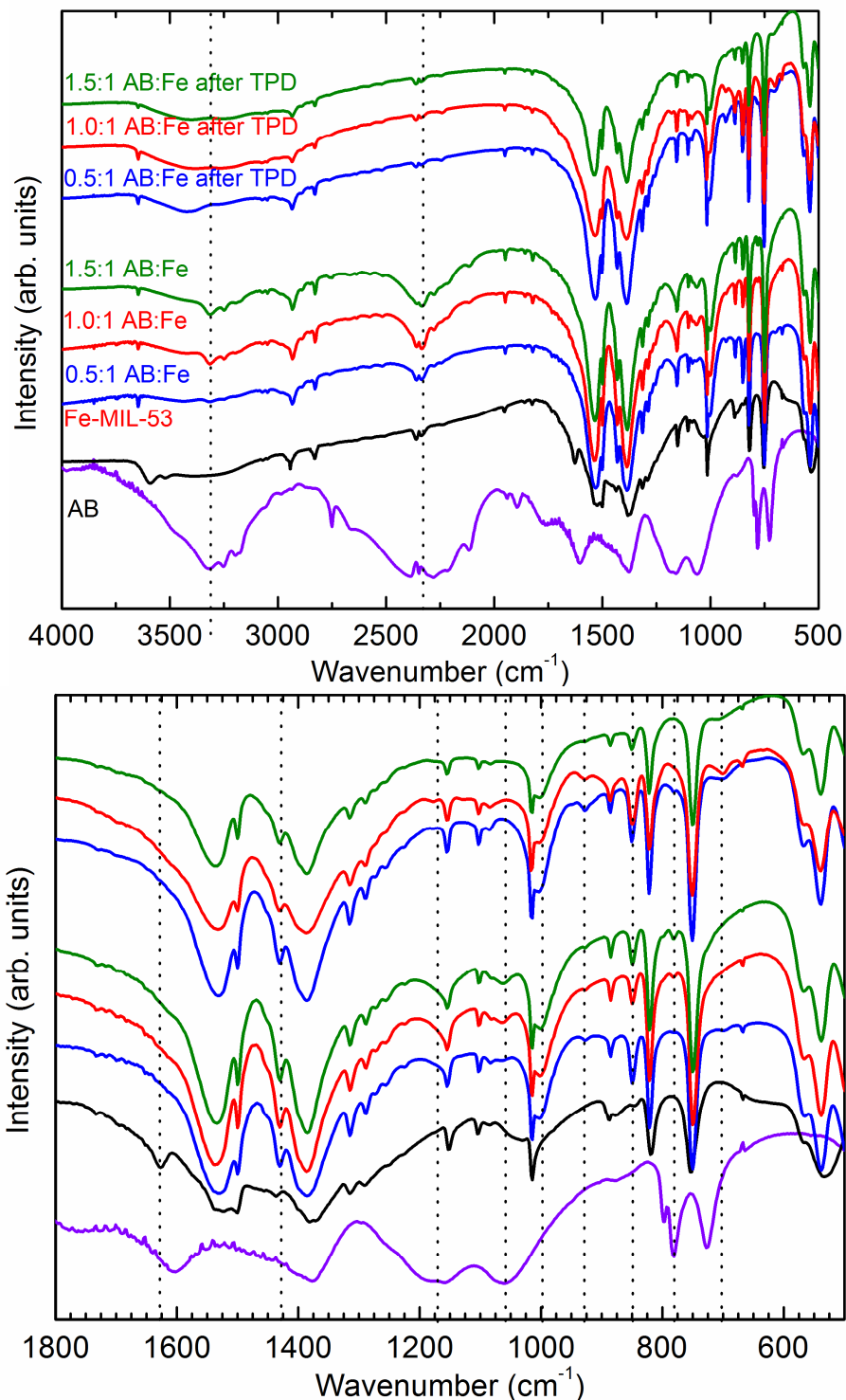
**Figure S2.** FTIR spectra of pristine AB, Fe-MIL-53, and AB loaded Fe-MIL-53 before and after thermal dehydrogenation. In pristine AB, the broad IR modes between 3200 cm^{-1} and 3500 cm^{-1}, and 2200 cm^{-1} and 2500 cm^{-1} correspond to the H–N and H–B stretching bonds, respectively. In addition, H–N scissor modes at 1602 cm^{-1} and 1376 cm^{-1}, H–B scissor mode at 1160 cm^{-1}, and

2

H- wagging modes at 1065 cm^{-1} and 727 cm^{-1} are observed. The mode at 781 cm^{-1} is assigned to B–N stretching.

The FTIR spectra of AB-MILs show combined IR modes related to the MOF and AB, but only very narrow H–N and H–B antisymmetric stretching IR modes around 3300 cm^{-1} and 2300 cm^{-1} respectively, is seen in infiltrated AB. This explains the significantly reduced AB–AB intermolecular interactions in the infiltrated AB molecules. After TPD run, the IR modes of H–N stretching bonds are seen at around 3400 cm^{-1}, however the H–B IR modes have disappeared, normally appear at around 2500 cm^{-1} in AB after 200 ^{o}C thermolysis. It is worth noticing that there are additional new IR modes at ~1010 cm^{-1}, ~925 cm^{-1}, 850 cm^{-1}, ~696 cm^{-1}, in AB-Fe-MIL before and after thermal desorption. The –OH vibration at ~1630 cm^{-1} in the MOF has disappeared in AB loaded MOFs. These are assigned to the coordination of B with oxygen functional groups in MOF pores **[I. Markova-Deneva, Infrared spectroscopy investigation of metallic nanoparticles based on copper, cobalt, and nickel synthesized through borohydride reduction method (review).** *Journal of the University of Chemical Technology and Metallurgy, 45, 4, 2010, 351-378***].** The B coordination with oxygen functional groups is also seen earlier in other AB loaded MOFs (AB-Mg-MOF-74 and AB-Zn-MOF-74) **[S. Gadipelli, J. Ford, W. Zhou, H. Wu, T. J. Udovic and T. Yildirim, Nanoconfinement and catalytic dehydrogenation of ammonia borane by magnesium-metal-organic framework-74,** *Chem. Eur. J.***, 2011, 17, 6043-6047. G. Srinivas, J. Ford, W. Zhou and T. Yildirim, Zn-MOF assisted dehydrogenation of ammonia borane: enhanced kinetics and clean hydrogen generation** *Int. J. Hydrogen Energy***, 2011, 37, 3633-3638.].**
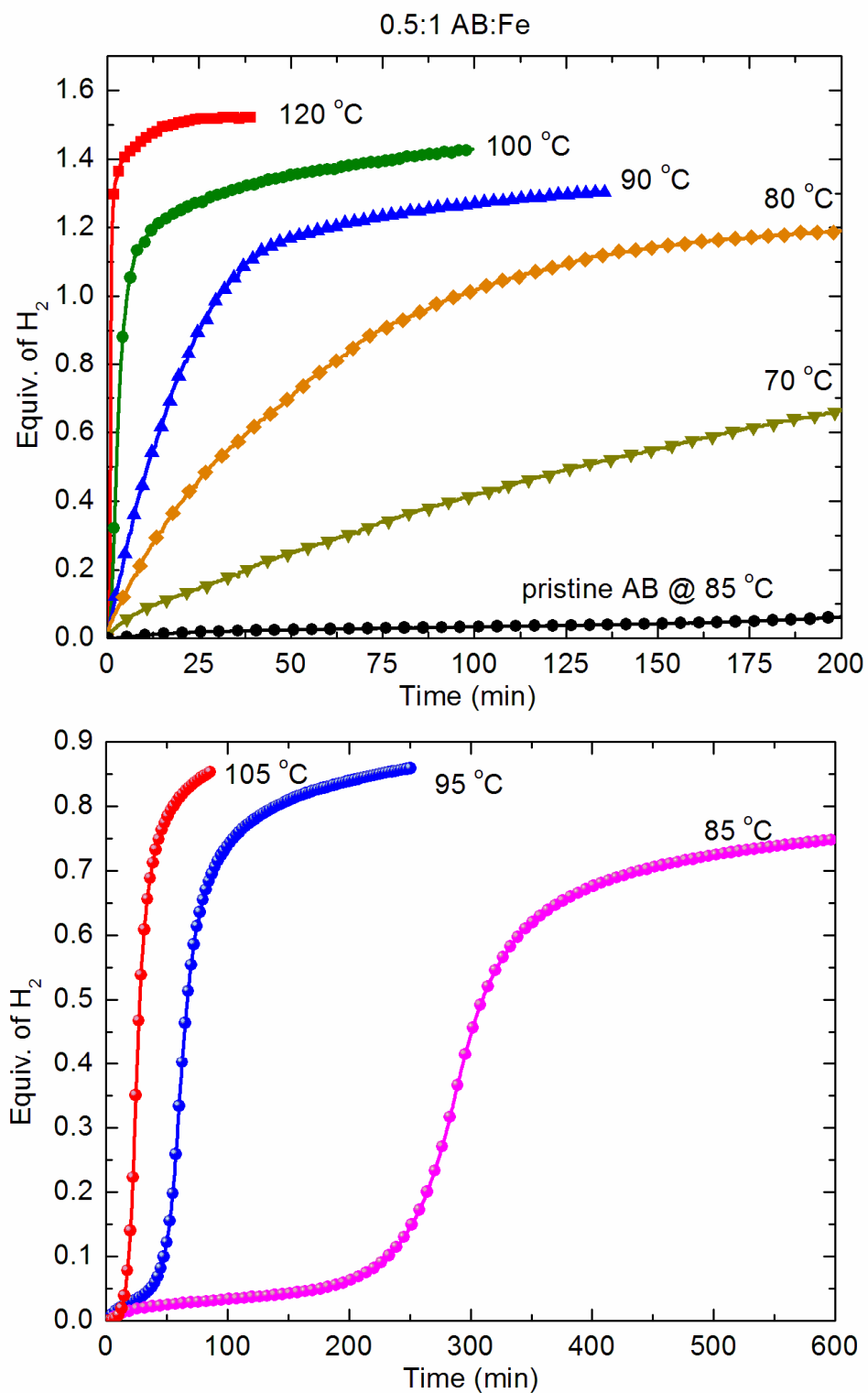
Figure S3. Isothermal hydrogen desorption kinetics at different constant temperatures of pristine AB and AB loaded Fe-MIL-53 with 0.5:1 AB:Fe.

4
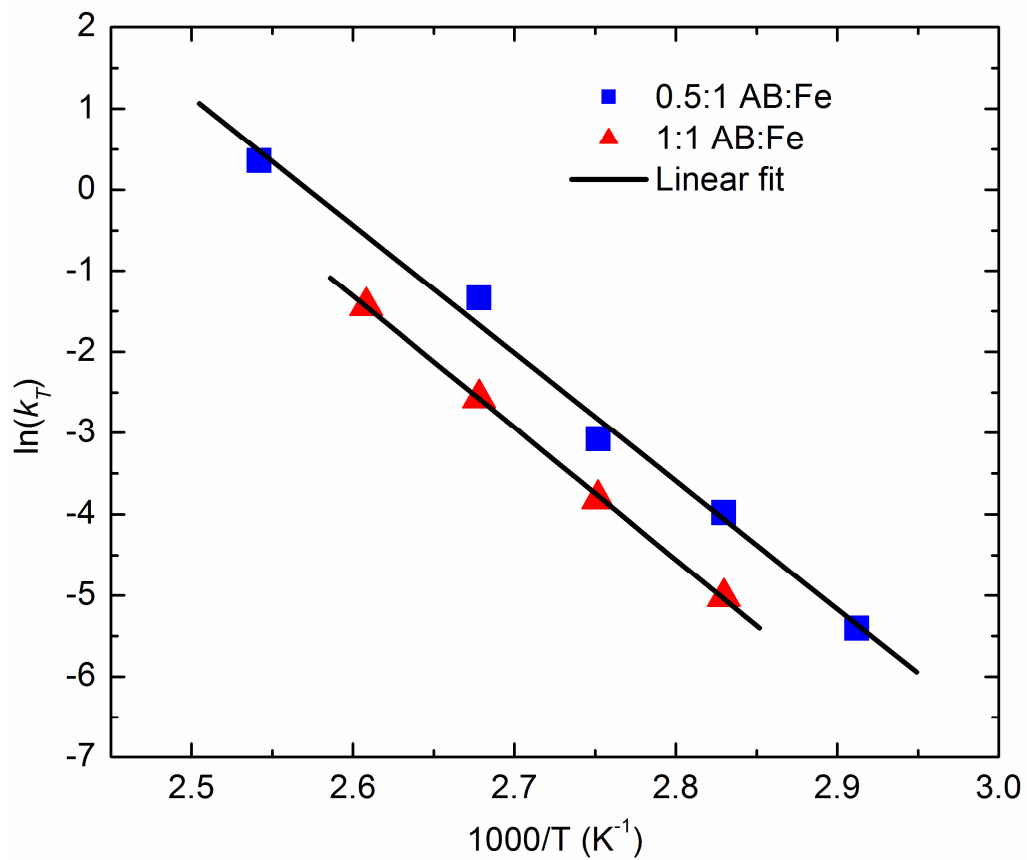
Figure S4. Arrhenius plots of the dehydrogenation kinetics of the AB-Fe-MIL-53 with 0.5:1 AB:Fe and 1:1 AB:Fe
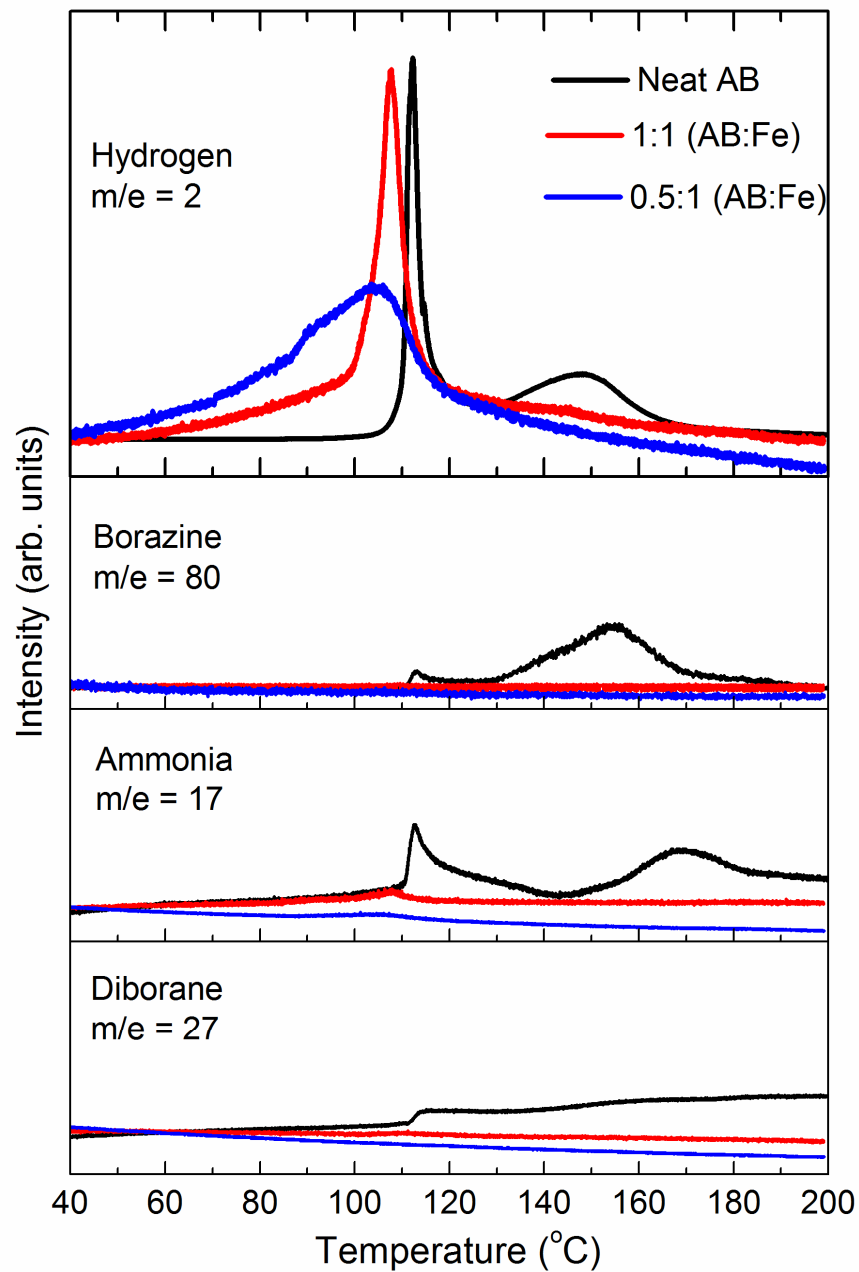
Figure S5. The mass spectroscopy data showing the clean hydrogen release from nanoconfined AB in Fe-MIL pores, whereas in pristine AB along with hydrogen the release of byproducts of ammonia, borazine and diborane is seen.

Figure S6. Photographs of pristine AB and Fe-MIL-53, and AB-Fe-MIL (1:1 AB:Fe) samples before and after thermal dehydrogenation (TGA) shows the extensive sample foaming is suppressed in nanoconfined AB sample.

7
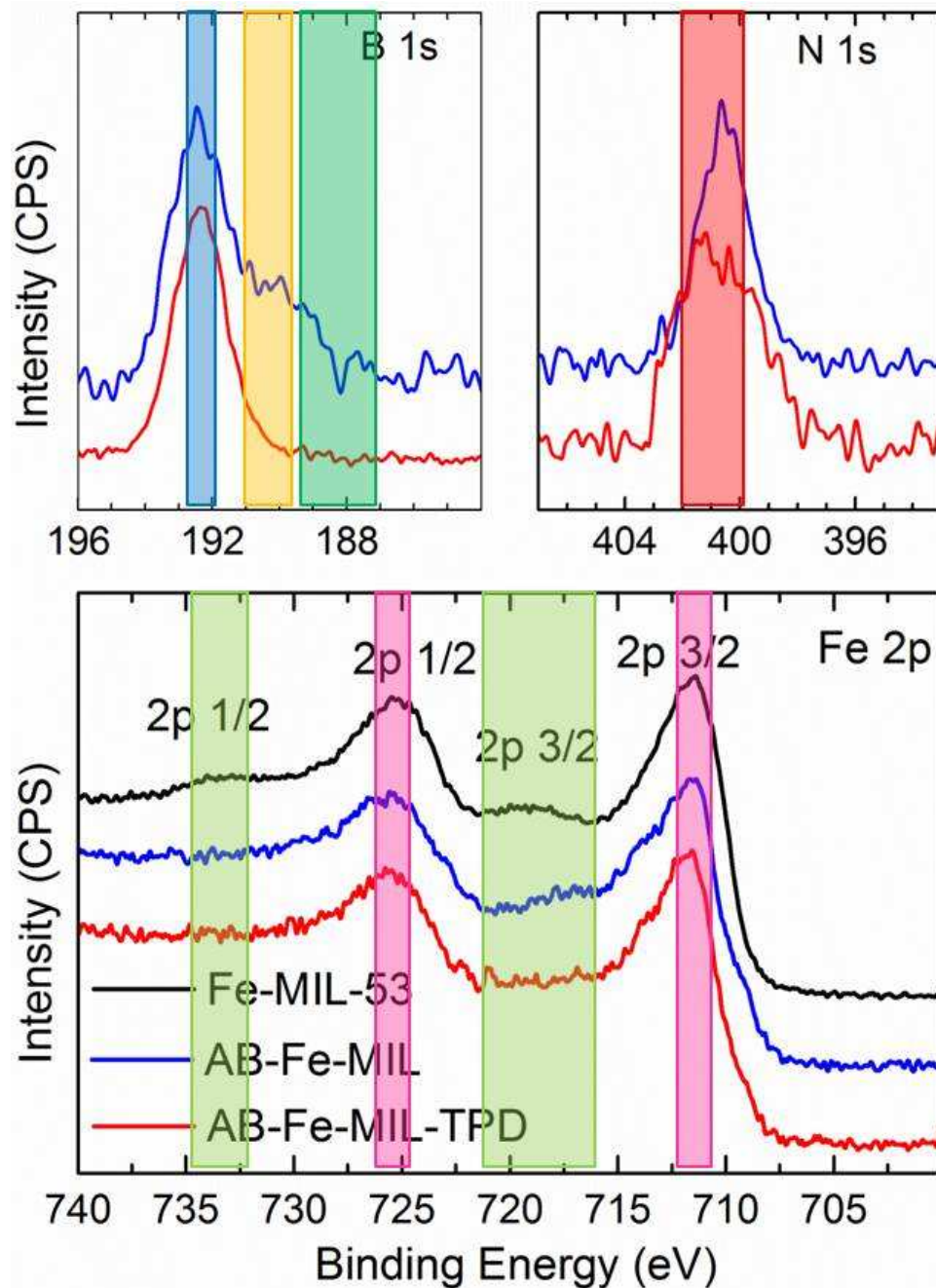
Figure S7. XPS B1s, N 1s, and Fe 2p core level spectra of Fe-MIL-53 and AB-Fe-MIL (1:1 AB:Fe) samples before and after thermal dehydrogenation at 200 °C.

In B 1s XPS core level spectra the BE of ~192.0 eV and ~188 eV are assigned to B–O and B–H bonds, respectively. The peak around 190 eV is assigned to B–N bonds, implying that not all the B–N bonds are broken in AB-Fe-MIL before thermal desorption [**J. Zhao, J. Shi, X. Zhang, F. Cheng, J. Liang, Z. Tao and J. Chen, A soft hydrogen storage material: poly(methyl acrylate)-confined ammonia borane with controllable dehydrogenation, Adv. Mater. 2010,**

22, 394–397.]. The B 1s and N 1s peaks in AB-Fe-MIL before and after thermal desorption also show no evidence of poly-(aminoborane) with binding energies of 191.1 eV for B 1s and 398.2 eV for N 1s or the counterpart boron nitride with 190.2 eV for B 1s and 397.9 eV for N 1s [R. A. Geanangel and J. W. Rabalais, **Evidence from mass spectra and X-ray photoelectron spectra concerning the structure of poly(aminoborane)**, *Inorganica Chimica Acta*, **1985, 97, 59-64**]. The broad N 1s peak between 403 eV and 398 eV (centered between 401 eV and 402 eV) in AB-Fe-MIL-TPD sample is assigned to $-NH_2-Fe$ and $-NH_2-O$ bonds [**Y. Wang, B. Li, Y. Zhou, D. Jia and Y. Song, CS-Fe(II,III) complex as precursor for magnetite nanocrystal**, *Polym. Adv. Technol.*, **2011, 22, 1681–1684**]. Fe 2p peaks of Fe-MIL-53 at BE ~711 eV and ~725 eV are assigned to Fe $2p_{3/2}$ and Fe $2p_{1/2}$ for iron(III) oxide, the additional satellite peaks at ~718 eV and ~730 eV are associated with Fe $2p_{3/2}$ and Fe $2p_{1/2}$, the spectra clearly resembles the Fe_2O_3 standard sample. The AB-Fe-MIL before and after thermal desorption exhibits similar spectra but with a shifted Fe $2p_{3/2}$ satellite peak to lower BE (~716 eV in AB-Fe-MIL) or no satellite peaks (in AB-Fe-MIL-TPD), respectively. It has been previously reported that Fe $2p_{3/2}$ for Fe_3O_4 ($FeO.Fe_2O_3$ with $Fe(II).Fe(III)$) does not have a satellite peak. In case of $Fe_{1-y}O$, the satellite peak for Fe $2p_{3/2}$ was observed at 715.5 eV [**T. Yamashita, P. Hayes, Analysis of XPS spectra of Fe^{2+} and Fe^{3+} ions in oxide materials**, *Appl. Surf. Sci.*, **2008, 254, 2441–2449.**].

First-Principles Calculations

In order to determine the hydrogen positions as well as the AB-molecule orientation and its location in MIL, we have performed first-principles structural optimization using Quantum Espresso Code PWSCF [P. Giannozzi et. al, J. Phys. Condens. Matter, 21, 395502 (2009)]. We used Vanderbilt-type ultrasoft pseudopotentials and the generalized gradient approximation (GGA) with the Perdew-Burke-Ernzerhof (PBE) exchange correlation. A kinetic energy cutoff of 544 eV and a *k*-point sampling with dk=0.03 Å^{-1} grid spacing were found to be enough for the total energy to converge within 0.5 meV/atom. AB molecules were introduced to the center of MIL structure assuming various initial orientations, followed by full atomic structural relaxation. The lattice parameters are kept constant at the experimental values but all the atomic positions are optimized until the maximum force is 0.005 eV/Ang. Below we list the optimized atomic positions for 0.5:1 loaded Fe-MIL. The simulated x-ray patterns shown in the text were obtained from these optimized atomic positions.

0.5:1 AB-Fe-MIL-53 Lattice Parameters and Optimized Atomic Positions

Cell: 21.2690 6.8839 6.9499 90.0000 114.6300 90.0000
ATOMIC_POSITIONS (crystal)
O   0.449176561 0.302978213 0.314712366
O   0.574583529 0.316060869 0.165448578

9

```
O    0.577091907  0.692695802   0.663903747
O    0.442258605  0.680144216   0.803812701
O    0.949170611  0.803056914   0.315249349
O    0.074719260  0.816387815   0.165617781
O    0.077123353  0.192807887   0.664017872
O    0.942119395  0.179984162   0.804111061
O    0.428209840  0.382435190   0.975869197
O    0.592483567  0.354296406   0.513093376
O    0.594819815  0.650856832   0.009924017
O    0.424296850  0.627861526   0.460233073
O    0.928266909  0.882069210  -0.023656119
O    0.092577062  0.854452556   0.513249088
O    0.094828620  0.151012623   0.010002310
O    0.924307203  0.128134094   0.460553502
O    1.012681950  0.893715445   0.745130216
O    1.013434427  0.129240470   0.245074787
O    0.512681709  0.393490392   0.744966516
O    0.513414824  0.629227833   0.244826761
C    0.334462678  0.268105248   0.044952018
C    0.685013612  0.246445770   0.431261393
C    0.691388954  0.716220551   0.928350311
C    0.326925666  0.682722786   0.543071407
C    0.834474939  0.767842429   0.045322997
C    0.185147297  0.746778415   0.431399537
C    0.191415818  0.216211977   0.928300442
C    0.826838043  0.182882292   0.543075357
C    0.308769650  0.236140250   0.198395672
C    0.709098546  0.206189127   0.275010745
C    0.717240933  0.742938126   0.773378498
C    0.302758631  0.717989592   0.699933437
C    0.808722491  0.735967218   0.198660186
C    0.209202533  0.706345608   0.275094139
C    0.217210181  0.243127543   0.773216146
C    0.802616548  0.217854878   0.699887513
C    0.238441513  0.209360428   0.141684556
C    0.779167626  0.174804951   0.330159458
C    0.787821893  0.767257951   0.830526812
C    0.232765133  0.749654589   0.644988596
C    0.738369112  0.709437481   0.141789633
C    0.279253449  0.674681775   0.330204233
C    0.287782163  0.267510972   0.830225859
C    0.732600145  0.249224809   0.644851085
C    0.409465141  0.319994653   0.115265677
C    0.611356827  0.308677312   0.365627361
C    0.615759118  0.683557045   0.864785469
```

C	0.403240595	0.659644783	0.606529464
C	0.909487314	0.819775218	0.115729189
C	0.111482098	0.808979206	0.365813318
C	0.115787493	0.183603741	0.864896793
C	0.903177949	0.159802489	0.606729526
H	0.344559968	0.234795777	0.364400042
H	0.672220910	0.205247596	0.109276173
H	0.681181218	0.744009520	0.606884016
H	0.340178815	0.726027167	0.864613102
H	0.844484180	0.734374637	0.364681653
H	0.172331556	0.705538666	0.109385049
H	0.181134928	0.244285559	0.606750553
H	0.839994328	0.225797766	0.864597417
H	0.219437268	0.184449516	0.263012478
H	0.797805394	0.148689849	0.208304331
H	0.807228596	0.787994053	0.709608842
H	0.214572257	0.782350980	0.766682586
H	0.719325651	0.684809071	0.263085788
H	0.297885994	0.648433818	0.208336225
H	0.307164704	0.288338732	0.709258748
H	0.714367078	0.281491441	0.766568749
H	0.468453906	0.312901130	0.698534505
H	0.542428685	0.745734802	0.285949504
H	0.968467030	0.813075401	0.698740602
H	1.042315793	0.246018949	0.286000679
H	0.532085141	0.090114889	0.728200257
H	0.437575291	1.031300055	0.862300473
H	0.500456786	0.872214405	0.637597878
H	0.408189835	0.237385099	0.638287586
H	0.478783959	0.065748811	0.477499825
H	0.374055367	0.983254198	0.554384945
H	0.032322019	0.590031013	0.729940483
H	0.937397358	0.530970511	0.862100769
H	0.000667893	0.372502596	0.637856473
H	0.908229141	0.737341229	0.638542389
H	-0.020754225	0.566860667	0.478855108
H	0.874273733	0.483133736	0.553849398
Fe	0.011796885	0.011845284	-0.007141601
Fe	1.011288915	0.002714805	0.489644268
Fe	0.511800338	0.511769911	-0.007347468
Fe	0.511267235	0.502557561	0.489396879
N	0.488490868	0.017421540	0.627751355
N	-0.011238667	0.517744897	0.628692102
B	0.423992104	1.066203532	0.679716094
B	0.924071674	0.566153160	0.679774739

11